Structural Stability of a Lightsail for Laser-Driven Propulsion

Dan-Cornelius Savu* and Andrew J. Higgins†
Department of Mechanical Engineering, McGill University, Montreal, Quebec, H3A 0C3, Canada

Directed energy propulsion—utilizing the ability of lasers to deliver energy over vast distances—has the potential to realize both rapid transit missions within the solar system, interstellar precursor missions, and true interstellar missions to other solar systems. This method of transportation proposes to use directed light energy onto a low areal density reflective foil (lightsail). The reflected beam is, based on first principle analyses, capable of accelerating spacecraft to speeds on the order of $\frac{1}{4}c$, where c is the speed of light. To achieve such great velocities in the near-field of the laser array necessitates very great accelerations and thus large dynamic loads being applied to the lightsail. In the case of an ideally smooth sail, the impinging light would undergo normal specular reflection, thereby ensuring the sail's shape and directional stability, but no material is ever perfectly flat on all scales. Because of the inevitable occurrence of non-uniform loading generated by surface irregularities, it remains uncertain whether a lightsail would retain its shape and not collapse or wrinkle when experiencing the large photon pressures that would be involved in laser-driven interstellar flight. This paper studies the shape stability of the lightsail using analytic models deriving from thin plate theory and finite-element models to construct a parameter map where zones of stability and instability are delimited for the key lightsail specifications of geometry, laser flux, and material properties.

Nomenclature

n	=	number of rigid sail elements
a_0	=	amplitude of perturbations
w	=	initial perturbations vertical displacement
ν	=	mode number of initial perturbations
c	=	speed of light in vacuum
I_0	=	light beam intensity
g_0	=	non-inertial D'Alembert vertical acceleration
L	=	working length
W	=	width
h	=	thickness
l	=	element length
A	=	discrete element in-plane area
A_c	=	cross-sectional area
d	=	diameter
$\mathbf{f}_i$	=	i^{th} element radiation force
f_0	=	flat element radiation force magnitude
I_G	=	moment of inertia about the center of mass
I	=	second moment of area
κ	=	curvature
E	=	material Young's modulus
T	=	boundary tension magnitude
$\mathbf{T}$	=	boundary tension vector
P	=	applied static transverse load
P_0	=	applied transverse load magnitude

*Undergraduate Research Assistant, Department of Mechanical Engineering, 817 Sherbrooke St. W., Student Member AIAA.
†Professor, Department of Mechanical Engineering, 817 Sherbrooke St. W., Senior Member AIAA.

E_{cr}	=	critical Young's modulus
$E_{\text{cr}_{\text{max}}}$	=	maximum critical Young's modulus value
T_{cr}	=	critical boundary tension
$T_{\text{cr}_{\text{max}}}$	=	maximum critical boundary tension value
ρ	=	density
M	=	bulk mass
$\mathcal{M}$	=	moment/torque
m	=	discrete element mass
x_i	=	x-position of the i^{th} element's center of mass
y_i	=	y-position of the i^{th} element's center of mass
θ_i	=	angular position of the i^{th} element with respect to the positive x-axis
z_i	=	elongation of the i^{th} element's rectilinear spring
k_{T}	=	torsional spring constant
k_{s}	=	rectilinear spring constant
l_{s}	=	rectilinear spring elongation at rest (always set to 0)
t	=	time
t_{final}	=	final simulation runtime
τ	=	time constant
$\mathcal{L}$	=	the Lagrangian
$\mathbf{q}$	=	vector of generalised coordinates with components q_i
$\mathbf{x}$	=	modified vector of generalised coordinates
$\mathbf{M}$	=	mass matrix
$\mathbf{f}$	=	forcing vector
$\hat{\mathbf{M}}$	=	modified mass matrix
$\hat{\mathbf{f}}$	=	modified forcing vector
$\mathbf{r}$	=	position vector
$\mathbf{n}$	=	normal vector

I. Introduction

Concentrating light energy onto a reflective foil to permit fast transportation within the solar system and beyond has been actively considered since the 1980s [1]. With the constant improvement of fiber optics within the telecommunication and laser machining industry, the laser-driven spacecraft is now steadily turning from concept to a present-day reality. Large light beams can now be made by constructing phased arrays of lasers using inexpensive optical components [2]. These propulsive loads can, in principle, accelerate spacecraft to speeds close to $\frac{1}{4}$ c, however, it is unclear how stable the system remains when under such great laser flux [2, 3].

The Lightsail directional or "beam-riding" stability has thus far been extensively studied in the literature. The directional stability of spacecraft propelled using spherical and hyperboloid shaped sails have been shown to be possible [4, 5], and the material composition of the sail has also been taken into consideration [6]. Directional stability has also been shown possible without the use of sail shape deformation by means of an engineered diffraction lightsail surface [7, 8]. Theses studies have assumed the lightsail to be either ideally flat or perfectly smooth, that is, absent of irregular deformations. Irregular deformations have been built into several other models in an attempt to quantify the influence of deformation upon the interstellar trajectory of the lightsail [9, 10]. Huang et al., for example, inquired in the deviation of the resultant solar radiation pressure (SRP) force due to lightsail deformation effects caused by wrinkling and billowing effects via the use of point cloud and triangular mesh methods. Structural analysis of the lightsail, considering beams and membranes has also been undertaken. Liu et al. for instance studied the attitude dynamics and the vibrations of a square lightsail supported by two beams each running across the lightsail's diagonal, which allowed them to neglect the detailed lightsail membrane vibrations and wrinkle effects [11]. Wong and Pellegrino, in a series of studies, inquired into the visible membrane wrinkling amplitude and wavelength growth when tension is gradually applied to the corners of an initially seemingly flat, square membrane [12–15]. Other studies concerning the problem of sail shape stability have also been undertaken for particular sail shapes [16, 17]. All attempts at providing stable sail configurations were not solely theoretical, however. Myrabo et al., for example, have conducted experimental investigations on the problem by subjecting lightsail prototypes to laser loads in vacuum [18]. Wong and Pellegrino also did their own series of in-laboratory experiments to validate their numerical results.

Thus far, no inquiry into the detailed vibrations and deformations of a lightsail under high photon radiation loading have been completed. In particular, no study on the growth of the inherent defects of the lightsail material due to the radiation loading have been done. Microscopic defects, though not visible to the naked eye, cannot be avoided during the manufacturing and deployment of the lightsail. Given that the defects prevent specular reflection on a macroscopic scale, the non-uniform nature of the resulting radiation pressure loads may precipitate the sail to both structural and dynamic failure. The present study revisits the question of lightsail shape stability with irregularities in mind by considering a first-principles approach to the problem. The purpose being to provide a general stability analysis irrespective of bulk sail geometry and encompassing a broad range of material properties. This should ultimately allow for flexibility of design as per mission requirements while still guaranteeing sail structural integrity.

II. Theoretical Considerations

As a preliminary consideration of the problem of a lightsail under radiation loading, the loading on a sinusoidally perturbed sail will be examined in a quasi-static analysis (see Fig. 1. for reference). The sail will initially be assumed to have a profile given by

$$\mathrm{w} = a_0 \sin\left(\frac{2\,\pi\,\nu\,x}{L}\right) \tag{1}$$

where ν is the mode number of the perturbation, which will be taken as whole and halved positive integers, i.e., $\nu = \frac{1}{2}, 1, \frac{3}{2}, 2, ...$ The acceleration of the sinusoidal lightsail can be found by integrating the forces acting on the sail in the y-direction:

$$\sum F_y = M\,g_0 \tag{2}$$

$$\int_0^L \frac{2I_0}{c}\,W\,\cos^2\theta\,\mathrm{d}x = g_0 \int_0^L \rho\,h\,W \frac{\mathrm{d}x}{\cos\theta} \tag{3}$$

where θ is the local angle of the lightsail.

Using the small angle approximations $\sin(\theta) \approx \theta \approx \frac{\mathrm{d}w}{\mathrm{d}x}$ and $\cos(\theta) \approx 1 - \frac{\theta^2}{2}$, the acceleration of the lightsail can be solved for

$$g_0 = \frac{2I_0}{c\,\rho\,h}\left[1 - 2\pi^2 n^2 \left(\frac{a_0}{L}\right)^2\right] \tag{4}$$

The second term in the brackets represents a decrement of lightsail acceleration due to the momentum of photons being scattered off the perturbed reflective surface. For the rest of this section, only the first-order approximation ($g_0 \approx \frac{2I_0}{c\,\rho\,h}$) will be retained.

For the remainder of this section, the analysis will be conducted in a non-inertial reference frame accelerating at g_0, with a body force term g_0 acting in the $-y$-direction on the mass elements of the lightsail in accordance with D'Alembert's principle. The moments acting on a point O located along the sail can be computed by conceptually cutting the lightsail at that point:

$$\begin{aligned}\sum \mathcal{M}_0 = -\mathcal{M}(x_0) &+ \int_{x_0}^L \frac{2I_0}{c}\,W\,\,(x - x_0)\cos^2\theta\mathrm{d}x \\ &- \int_{x_0}^L \rho\,h\,g_0\,W\,\,(x - x_0)\,\frac{\mathrm{d}x}{\cos\theta} - \int_{x_0}^L \frac{2I_0}{c}\,W\,\,(w_0 - w)\cos\theta\sin\theta\,\mathrm{d}x + T\,w(x_0)\cos\theta.\end{aligned} \tag{5}$$

The tension T is tangent to the L end of the lightsail, however, given the small amplitude of the sinusoidal deformation, the dynamic contribution of its vertical component is neglected. Again using the small angle approximations and retaining only first order terms, Eq. (5) can be integrated to yield.

The above equation defines a state of static equilibrium of the lightsail: The net moment applied to the sail by acceleration body-force term and the radiation pressure is balanced by a material moment resulting from bending of the lightsail. The elastic modulus necessary to provide the moment $\mathcal{M}_0(x_0)$ can be found from the relation

$$\mathcal{M} = E\,I\,\kappa \tag{6}$$

where E is the elastic modulus (Young's modulus), I is the moment of area of cross-section of the sail about the z-axis, and κ is the curvature of the deformed lightsail. Using $\kappa \approx \frac{\mathrm{d}^2 w}{\mathrm{d}x^2}$, the curvature and thus bending moment can be solved for.

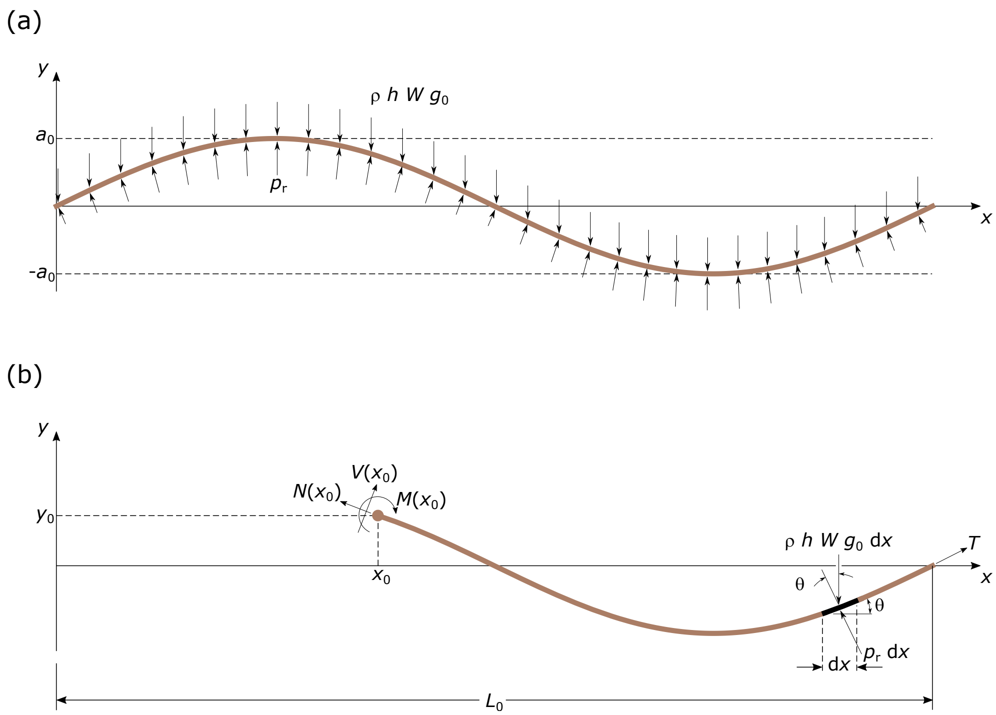

Fig. 1 Model using in analytic model for lightsail stability. (a) Force analysis on entire lightsail. (b) Moment analysis about point on lightsail located at x_0.

By comparing the applied moments due to radiation and acceleration (in the non-inertial frame) and the moments due to bending of a stiff sail and applied tension, an indication of the lightsail material stability can be obtained. For example, if the actual lightsail's bending stiffness or tension greatly exceeds the values applied by radiation and acceleration, it is plausible that the sail remains stable. If the moments caused by radiation pressure greatly exceed the bending moment of the lightsail, however, the lightsail is likely to undergo further–potentially catastrophic–deformation. From these considerations, it is possible to define a critical value of elastic modulus (in the absence of tension, i.e., $T = 0$)

$$E_{\mathrm{cr}} = -\frac{3}{2}\left(\frac{2I_0}{c}\right)\frac{a_0 L^2}{\pi^2\,\nu^2\,h^3}\sin\left(\frac{2\,\pi\,\nu\,x_0}{L}\right), \text{ with} \tag{7}$$

$$E_{\mathrm{cr_{MAX}}} = \frac{3}{2}\left(\frac{2I_0}{c}\right)\frac{a_0 L^2}{\pi^2\,\nu^2\,h^3}, \tag{8}$$

where the extrema values, $E_{\mathrm{cr_{m}athrmmax}}$ occurring at the peaks and troughs of the sinusoid. For the case of tension (in the absence of bending stiffness), the critical value of tension (per unit width of the lightsail) can be found

$$T_{\mathrm{cr}} = -\frac{1}{2}\left(\frac{2I_0}{c}\right) a_0 \sin\left(\frac{2\,\pi\,\nu\,x_0}{L}\right), \text{ with} \tag{9}$$

$$T_{\mathrm{cr_{max}}} = \frac{1}{2}\left(\frac{2I_0}{c}\right) a_0. \tag{10}$$

The results of this quasi-static analysis provide a candidate for the functional form of the relation between material properties (i.e., elastic modulus), perturbation amplitude and wavelength, and the radiation intensity. The results of Eq. 10 also suggest a critical value of the tension necessary to prevent the development of instability. These findings will help guide the computational simulations of the full lightsail dynamics that are found in the remainder of the paper.

III. Numerical Considerations

A. Rigid-Elements Lightsail Model

With the intent of achieving the rapid transit of a small-scale spacecraft equipped with a 1 meter sail to Mars (1 AU) in 30 minutes or to 0.3 c for interstellar flight within three minutes, the mission at launch would require the use of a $0.1 - 100\,\mathrm{GW}$ laser load [2, 3]. The stability of the lightsail at launch is here analyzed by first considering a rectangular sail with dimensions $L \times L \times h$ where $L = 1$ m and h is the sail's thickness. The sail was then divided into n equal slices of length $l = L/n$ and mass m, each attached together via frictionless hinges (see Fig. 2). The system was further subjected to a *uniform impinging photon pressure load distribution*. This uniform pressure results in the presence of concentrated forces along the center of mass (CoM) of each individual slice. Specular reflection is assumed to occur between an individual photon and a sail element given the idealized flat surface of each slice which produces resultant forces that are parallel to the normal of their respective element. In the limit where the number of rigid slice elements is very large (i.e., when $n \rightarrow \infty$) this assumption holds true because of the infinitesimal length of each element. The force imparted to the i^{th} element by the photon pressure is thus

$$\mathbf{f}_i = \frac{2I_0}{c} A \cos^2 \theta_i \mathbf{n} \tag{11}$$

where I_0 is the laser beam intensity, $A = L \times l$ is the slice element area, and θ_i is the i^{th} element's inclination with respect to the horizontal.

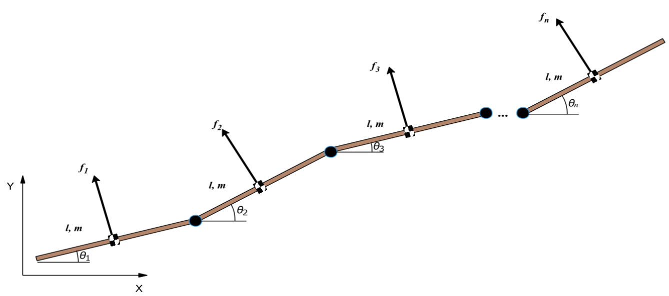

Fig. 2 Finite-Element (FE) model of the lightsail using rigid slices and frictionless connections.

To analyze the dynamical behavior of the system, the Lagrangian formalism of mechanics was used. First, the Lagrangian of the system was constructed alongside its constraints (note that $I_G = \frac{1}{12}ml^2$ is the moment of inertia of the sail element about its respective center of mass).

$$\mathcal{L}_{\text{rigid}} = \frac{1}{2} m \sum_{j=1}^{n} \left(\dot{x}_j^2 + \dot{y}_j^2\right) + \frac{1}{2} I_G \sum_{j=1}^{n} \dot{\theta}^2, \text{ with} \tag{12}$$

$$x_j = x_1(t) + \frac{l}{2}\left(\cos\theta_1 + 2\sum_{i=2}^{j-1}\cos\theta_i + \cos\theta_j\right), \text{ and} \tag{13}$$

$$y_j = y_1(t) + \frac{l}{2}\left(\sin\theta_1 + 2\sum_{i=2}^{j-1}\sin\theta_i + \sin\theta_j\right). \tag{14}$$

Further, the non-conservative generalized forces that arise due to the radiation forces, $\mathbf{f}_i$, are

$$Q_j = \sum_{i=1}^{n} \mathbf{f}_i \cdot \frac{\partial \mathbf{r}_i}{\partial q_j}, \text{ with} \tag{15}$$

$$\mathbf{f}_i = f_0 \cos^2\theta_i \left(-\sin\theta_i, \cos\theta_i, 0\right), \text{ and}$$

$$f_0 = \frac{2I_0}{c} l L, \quad \mathbf{r}_i = (x_i, y_i, 0)\,.$$

Using the above terms, the equations of motion (EOM) of the system was derived using the Euler-Lagrange equations

$$\frac{\mathrm{d}}{\mathrm{d}t}\left(\frac{\partial L}{\partial \dot{q}_j}\right) - \frac{\partial L}{\partial q_j} = Q_j \tag{16}$$

where $q_i = x_1,\ y_1,\ \theta_1,\ \ldots,\ \theta_n$ are the generalized coordinates of the system encapsulated in the vector of unknowns $\mathbf{q}_{\text{rigid}} = [\mathbf{x_1},\ \mathbf{y_1},\ \theta]^{\mathbf{T}}$. After applying the derivatives, we obtain the following equations:

- x_1 equation of motion for the torsion model

$$-2n\ddot{x}_1 + \sum_{j=1}^{n} a_j^{xy} \sin\theta_j \ddot{\theta}_j \;=\; -\sum_{j=1}^{n} a_j^{xy} \cos\theta_j \dot{\theta}_j^2 + \frac{2}{m} f_0 \sum_{j=1}^{n} \sin\theta_j \cos^2\theta_j \tag{17}$$

- y_1 equation of motion for the torsion model

$$2n\ddot{y}_1 + \sum_{j=1}^{n} a_j^{xy} \cos\theta_j \ddot{\theta}_j \;=\; \sum_{j=1}^{n} a_j^{xy} \sin\theta_j \dot{\theta}_j^2 + \frac{2}{m} f_0 \sum_{j=1}^{n} \cos^3\theta_j \tag{18}$$

- θ_1 equation of motion for the torsion model

$$\begin{aligned} -6\,(n-1) l \sin\theta_1 \ddot{x}_1 + 6\,(n-1)\, l \cos\theta_1 \ddot{y}_1 + \sum_{j=1}^{n} a_j^{\theta_1} \cos\left(\theta_1 - \theta_j\right) \ddot{\theta}_j \;=\; \\ + \frac{12}{m}\frac{l}{2} f_0 \sum_{j=2}^{n} \left(\sin\theta_1 \sin\theta_j \cos^2\theta_j + \cos\theta_1 \cos^3\theta_j\right) - \sum_{j=1}^{n} a_j^{\theta_1} \sin\left(\theta_1 - \theta_j\right) \dot{\theta}_j^2 \end{aligned} \tag{19}$$

- θ_k equations of motion for the torsion model where $k = 2,\ 3,\ 4,\ \ldots,\ n-1$

$$\begin{aligned} -6(2n-2k)+1) l \sin\theta_k \ddot{x}_1 + 6(2n-2k+1) l \cos\theta_k \ddot{y}_1 + \sum_{j=1}^{n} a_{kj}^{\theta_k} \cos\left(\theta_k - \theta_j\right) \ddot{\theta}_j \;=\; \\ + \frac{12}{m}\frac{l}{2} f_0 \left(\sin^2\theta_k \cos^2\theta_k + \cos^4\theta_k\right) + \frac{12}{m} l f_0 \sum_{j=k+1}^{n} \left(\sin\theta_k \sin\theta_j \cos^2\theta_j + \cos\theta_k \cos^3\theta_j\right) \\ - \sum_{j=1}^{n} a_{kj}^{\theta_k} \sin\left(\theta_k - \theta_j\right) \dot{\theta}_j^2 \end{aligned} \tag{20}$$

- θ_n equation of motion for the torsion model

$$\begin{aligned} -6l \sin\theta_n \ddot{x}_1 + 6l \cos\theta_n \ddot{y}_1 + \sum_{j=1}^{n} a_{nj}^{\theta_n} \cos\left(\theta_n - \theta_j\right) \ddot{\theta}_j \;=\; -\sum_{j=1}^{n} a_{kj}^{\theta_k} \sin\left(\theta_k - \theta_j\right) \dot{\theta}_j^2 \\ + \frac{12}{m}\frac{l}{2} f_0 \left(\sin^2\theta_n \cos^2\theta_n + \cos^4\theta_n\right) \end{aligned} \tag{21}$$

with the auxiliary coefficients

$$a_j^{xy} = \begin{cases} (n-1)\,l & \text{for } j=1 \\ (2n-2j+1)l & \text{for } j>1 \end{cases}$$

$$a_j^{\theta_1} = \begin{cases} 3(n-1)l^2 + l^2 & \text{for } j=1 \\ 3(2n-2j+1)l^2 & \text{for } j>1 \end{cases}$$

$$a_{kj}^{\theta_k} = \begin{cases} 3(2n-2k+1)l^2 & \text{for } j=1 \\ 6(2n-2k+1)l^2 & \text{for } 1<j<k \\ 12(n-k)l^2+4l^2 & \text{for } j=k \\ 6(2n-2j+1)l^2 & \text{for } j>k \end{cases}$$

B. Torsion Lightsail Model

To include the material bending stiffness of the lightsail within the study, the finite-element model was further refined by attaching torsional spring elements with stiffness constant $k_{\mathrm{T}} = EI/l$ to the hinges connecting the rigid slices together (see Fig. 3). To see a full derivation of this discrete torsional spring constant from the moment-curvature relation, the reader is referred to [19]. EI here stands for the *flexural modulus* of each individual slice with E being the sail material elastic modulus. Here, I, the second moment of area of each rigid element is as previously encountered in the above theoretical section,

$$EI = E\left(\frac{1}{12}Lh^3\right). \tag{22}$$

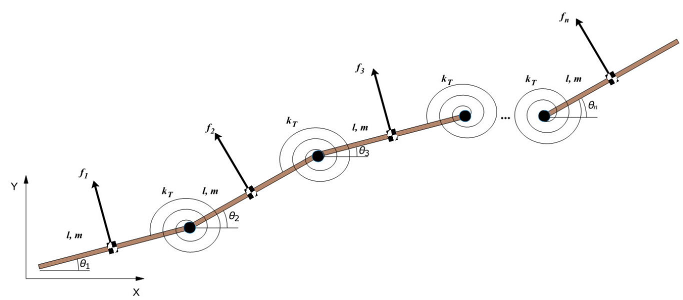

Fig. 3 Finite-element model refinement using torsional spring elements to simulate material strength.

Employing the same variational approach as for the rigid lightsail model, the Lagrangian of the system now is slightly modified with the appearance of a potential energy term arising from the additional presence of the linear torsional springs:

$$\mathcal{L}_{\text{torsion}} = \frac{1}{2}m\sum_{j=1}^{n}\left(\dot{x}_j^2+\dot{y}_j^2\right) + \frac{1}{2}I_{\mathrm{G}}\sum_{j=1}^{n}\dot{\theta}^2 - \frac{1}{2}k_{\mathrm{T}}\sum_{j=2}^{n}\left(\theta_j-\theta_{j-1}\right)^2 \tag{23}$$

Coupling equation (23) with equations (13), (14), and (15) and applying the Euler-Lagrange equations, we obtain a new set of ordinary differential equations (ODEs) describing this refined lightsail model:

- x_1 equation of motion for the torsion model

$$-2n\ddot{x}_1 + \sum_{j=1}^{n} a_j^{xy}\sin\theta_j\ddot{\theta}_j = -\sum_{j=1}^{n} a_j^{xy}\cos\theta_j\dot{\theta}_j^2 + \frac{2}{m}f_0\sum_{j=1}^{n}\sin\theta_j\cos^2\theta_j \tag{24}$$

- y_1 equation of motion for the torsion model

$$2n\ddot{y}_1 + \sum_{j=1}^{n} a_j^{xy}\cos\theta_j\ddot{\theta}_j = \sum_{j=1}^{n} a_j^{xy}\sin\theta_j\dot{\theta}_j^2 + \frac{2}{m}f_0\sum_{j=1}^{n}\cos^3\theta_j \tag{25}$$

- θ_1 equation of motion for the torsion model

$$-6\,(n-1) l \sin\theta_1 \ddot{x}_1 + 6\,(n-1)\, l\cos\theta_1 \ddot{y}_1 + \sum_{j=1}^{n} a_j^{\theta_1} \cos\left(\theta_1 - \theta_j\right)\ddot{\theta}_j \;=\; + \frac{12}{m}\frac{l}{2} f_0 \sum_{j=2}^{n}\left(\sin\theta_1 \sin\theta_j \cos^2\theta_j + \cos\theta_1 \cos^3\theta_j\right) - \sum_{j=1}^{n} a_j^{\theta_1} \sin\left(\theta_1 - \theta_j\right)\dot{\theta}_j^2 + \frac{12}{m} k_{\mathrm{t}}\left(\theta_2 - \theta_1\right) \tag{26}$$

- θ_k equations of motion for the torsion model where $k = 2, 3, 4, \ldots, n-1$

$$-6(2n-2k)+1) l \sin\theta_k \ddot{x}_1 + 6(2n-2k+1) l \cos\theta_k \ddot{y}_1 + \sum_{j=1}^{n} a_{kj}^{\theta_k}\cos\left(\theta_k - \theta_j\right)\ddot{\theta}_j \;=\; + \frac{12}{m}\frac{l}{2} f_0\left(\sin^2\theta_k\cos^2\theta_k + \cos^4\theta_k\right) + \frac{12}{m} l f_0 \sum_{j=k+1}^{n}\left(\sin\theta_k\sin\theta_j\cos^2\theta_j + \cos\theta_k\cos^3\theta_j\right) - \sum_{j=1}^{n} a_{kj}^{\theta_k}\sin\left(\theta_k - \theta_j\right)\dot{\theta}_j^2 - \frac{12}{m} k_{\mathrm{t}}\left(\theta_k - \theta_{k-1}\right) + \frac{12}{m} k_{\mathrm{t}}\left(\theta_{k+1} - \theta_k\right) \tag{27}$$

- θ_n equation of motion for the torsion model

$$-6l\sin\theta_n\ddot{x}_1 + 6l\cos\theta_n\ddot{y}_1 + \sum_{j=1}^{n} a_{nj}^{\theta_n}\cos\left(\theta_n - \theta_j\right)\ddot{\theta}_j \;=\; -\sum_{j=1}^{n} a_{kj}^{\theta_k}\sin\left(\theta_k - \theta_j\right)\dot{\theta}_j^2 + \frac{12}{m}\frac{l}{2} f_0\left(\sin^2\theta_n\cos^2\theta_n + \cos^4\theta_n\right) - \frac{12}{m} k_{\mathrm{t}}\left(\theta_k - \theta_{k-1}\right) \tag{28}$$

with the same auxiliary coefficients a_j^{xy}, $a_j^{\theta_1}$, and $a_{kj}^{\theta_k}$ as in the rigid case. Note that the only difference between the equations of motion of the torsion and rigid models are the addition of the torsional spring restoring moments highlighted in red in the RHS of equations (26) to (28). For the sake of completion and clarity, however, the whole set of ODEs was nevertheless reiterated above.

C. Tension and Torsion (TnT) Lightsail Model

To include both bending stiffness *and* tensile, linear stiffness of the material, we lightsail FE model was further refined to include the presence of rectilinear springs with stiffness constant $k_{\mathrm{s}} = (n-1)\frac{EhW}{L}$ and initially/rest length l_{s}. Further, to simulate a *pre-tensed* sail, boundary tension has been applied at both ends of the discretized lightsail. This new model is depicted in Fig. 4. The reader is referred to Appendix section B for a validation of this model against common wave theory.

The mathematics of this new model now considerable increase in complexity since, to keep track of the rectilinear spring deformation, we need to include an additional set of generalized coordinates $\boldsymbol{z} = [z_1, \ldots, z_{n-1}]^{\mathrm{T}}$ alongside the previous set of coordinates x_1, y_1, and $\boldsymbol{\theta} = [\theta_1, \ldots, \theta_n]^{\mathrm{T}}$. This makes for a full vector of generalized coordinates $\boldsymbol{q}_{\mathrm{TnT}} = [x_1, y_1, \boldsymbol{\theta}, \boldsymbol{z}]^T$ which contains $2n+1$ equations instead of the previous $n+2$. Given the additional presence of rectilinear springs, the Lagrangian of the system was also modified with another potential energy term:

$$\mathcal{L}_{\mathrm{TnT}} = \frac{1}{2} m \sum_{j=1}^{n}\left(\dot{x}_j^2 + \dot{y}_j^2\right) + \frac{1}{2} I_{\mathrm{G}} \sum_{j=1}^{n}\dot{\theta}^2 - \frac{1}{2} k_{\mathrm{T}} \sum_{j=2}^{n}\left(\theta_j - \theta_{j-1}\right)^2 - \frac{1}{2} k_{\mathrm{s}} \sum_{j=1}^{n-1} z_j^2. \tag{29}$$

The constraint equation is also revised; to relate the coordinates of each element's center of mass to the first element's coordinate (x_1, y_1), we now need to take into account the length of the springs $(l_{\mathrm{s}} + z_k)$ in addition to the length of each rigid element:

$$x_j = x_1(t) + \left(\frac{l}{2} + l_s + z_1\right)\cos\theta_1 + \sum_{i=2}^{j-1}\left\{(l + l_s + z_i)\cos\theta_i\right\} + \frac{l}{2}\cos\theta_j; \tag{30}$$

$$y_j = y_1(t) + \left(\frac{l}{2} + l_s + z_1\right)\sin\theta_1 + \sum_{i=2}^{j-1}\left\{(l + l_s + z_i)\sin\theta_i\right\} + \frac{l}{2}\sin\theta_j. \tag{31}$$

Given the inclusion of boundary tension, the generalized force components are also modified:

$$Q_j = -\mathrm{T}(\cos\theta_1, \sin\theta_1, 0)\cdot\frac{\partial \mathbf{r}_{T_1}}{\partial q_j} + \sum_{i=1}^{n}\mathbf{f}_i\cdot\frac{\partial \mathbf{r}_i}{\partial q_j} + \mathrm{T}(\cos\theta_n, \sin\theta_n, 0)\cdot\frac{\partial \mathbf{r}_{T_n}}{\partial q_j}, \text{ where} \tag{32}$$

$$\mathbf{r}_{T_1} = \left(x_1 - \frac{l}{2}\cos\theta_1,\ y_1 - \frac{l}{2}\sin\theta_1,\ 0\right), \quad \text{and} \quad \mathbf{r}_{T_n} = \left(x_n + \frac{l}{2}\cos\theta_n,\ y_n + \frac{l}{2}\sin\theta_n,\ 0\right);$$

$$\mathbf{T}_1 = T(-\cos\theta_1,\ -\sin\theta_1,\ 0), \quad \text{and} \quad \mathbf{T}_n = T(\cos\theta_n,\ \sin\theta_n,\ 0);$$

with $\mathbf{f}_i$ and $\mathbf{r}_i$ as in the previous models.

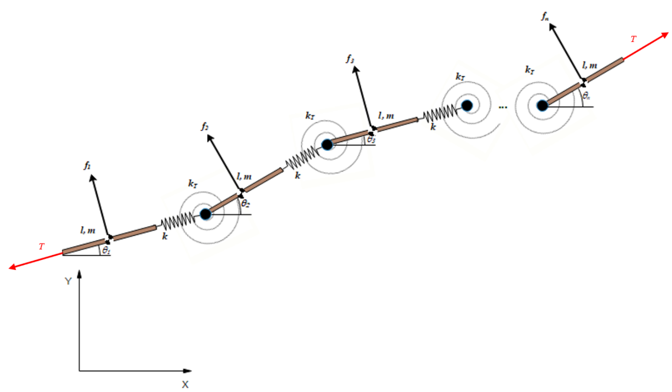

Fig. 4 Final FE model refinement including the addition of linear spring elements and boundary tension forces.

Applying the Euler-Lagrange variational equation using equations (29) through to (32) and simplifying ultimately yields a system of strongly coupled ODEs of size $2n + 1$:

- x_1 equation of motion for the TnT model

$$\begin{aligned} -2n\ddot{x}_1 + \sum_{j=1}^{n} A_j^{xy}\sin\theta_j\ddot{\theta}_j - \sum_{j=1}^{n-1} B_j^{xy}\cos\theta_j\ddot{z}_j \;=\; & -\sum_{j=1}^{n} A_j^{xy}\cos\theta_j\dot{\theta}_j^2 - 2\sum_{j=1}^{n-1} B_j^{xy}\sin\theta_j\dot{z}_j\dot{\theta}'_j \\ & + \frac{2}{m}f_0\sum_{j=1}^{n}\sin\theta_j\cos^2\theta_j + \frac{2}{m}T\left(\cos\theta_1 - \cos\theta_n\right) \end{aligned} \tag{33}$$

- y_1 equation of motion for the TnT model

$$\begin{aligned} 2n\ddot{y}_1 + \sum_{j=1}^{n} A_j^{xy}\cos\theta_j\ddot{\theta}_j + \sum_{j=1}^{n-1} B_j^{xy}\sin\theta_j\ddot{z}_j \;=\; & \sum_{j=1}^{n} A_j^{xy}\sin\theta_j\dot{\theta}_j^2 - 2\sum_{j=1}^{n-1} B_j^{xy}\cos\theta_j\dot{z}_j\dot{\theta}'_j \\ & + \frac{2}{m}f_0\sum_{j=1}^{n}\cos^3\theta_j + \frac{2}{m}T\left(\sin\theta_n - \sin\theta_1\right) \end{aligned} \tag{34}$$

- z_k equations of motion for the TnT model where $k = 1,\ 2,\ 3,\ \ldots,\ n-1$

$$
\begin{aligned}
2(n-k)\cos\theta_k\ddot{x}_1 + 2(n-k)\sin\theta_k\ddot{y}_1 + \sum_{j=1}^{n} A^{z}_{kj}\sin\left(\theta_k-\theta_j\right)\ddot{\theta}_j + \sum_{j=1}^{n-1} B^{z}_{kj}\cos\left(\theta_k-\theta_j\right)\ddot{z}_j \ &= \\
+\frac{2}{m}f_0\sum_{j=k+1}^{n}\left(\sin\theta_k\cos^3\theta_j - \cos\theta_k\sin\theta_j\cos^2\theta_j(t)\right) + \frac{2}{m}T\left(\sin\theta_n\sin\theta_k+\cos\theta_n\cos\theta_k\right) \\
+\sum_{j=1}^{n} A^{z}_{kj}\cos\left(\theta_k-\theta_j\right)\dot{\theta}_j^2 - 2\sum_{j=1}^{n-1} B^{z}_{kj}\sin\left(\theta_k-\theta_j\right)\dot{z}_j\dot{\theta}_j - \frac{2}{m}k_{\mathrm{s}}z_k
\end{aligned}
\tag{35}
$$

- θ_1 equation of motion for the TnT model

$$
\begin{aligned}
-6\left(n-1\right)\left(l+2l_{\mathrm{s}}+2z_1\right)\sin\theta_1\ddot{x}_1 + 6\left(n-1\right)\left(l+2l_{\mathrm{s}}+2z_1\right)\cos\theta_1\ddot{y}_1 \\
+\sum_{j=1}^{n} A^{\theta_1}_{j}\cos\left(\theta_1-\theta_j\right)\ddot{\theta}_j - \sum_{j=1}^{n-1} B^{\theta_1}_{j}\sin\left(\theta_1-\theta_j\right)\ddot{z}_j \ &= \\
+\frac{12}{m}\left(\frac{l}{2}+\mathrm{ls}+z_1\right)f_0\sum_{j=2}^{n}\left(\sin\theta_1\sin\theta_j\cos^2\theta_j+\cos\theta_1\cos^3\theta_j\right) \\
+\frac{12}{m}\left(\frac{l}{2}+\mathrm{ls}+z_k\right)T\left(\sin\theta_n\cos\theta_1-\sin\theta_1\cos\theta_n\right)+\frac{12}{m}k_{\mathrm{t}}\left(\theta_2-\theta_1\right) \\
-\sum_{j=1}^{n} A^{\theta_1}_{j}\sin\left(\theta_1-\theta_j\right)\dot{\theta}_j^2 - 2\sum_{j=1}^{n-1} B^{\theta_1}_{j}\cos\left(\theta_1-\theta_j\right)\dot{z}_j\dot{\theta}_j
\end{aligned}
\tag{36}
$$

- θ_k equations of motion for the TnT model where $k = 2,\ 3,\ 4,\ \ldots,\ n-1$

$$
\begin{aligned}
-6\left[(2n-2k)\ +1)l+2(n-k)l_{\mathrm{s}}+2(n-k)z_k\sin\theta_k\ddot{x}_1 + 6\left[(2n-2k+1)l+2(n-k)l_{\mathrm{s}}+2(n-k)z_k\right]\cos\theta_k\ddot{y}_1 \\
+\sum_{j=1}^{n} A^{\theta_k}_{kj}\cos\left(\theta_k-\theta_j\right)\ddot{\theta}_j - \sum_{j=1}^{n-1} B^{\theta_k}_{kj}\sin\left(\theta_k-\theta_j\right)\ddot{z}_j \ &= \\
+\frac{12}{m}\frac{l}{2}f_0\left(\sin^2\theta_k\cos^2\theta_k+\cos^4\theta_k\right)+\frac{12}{m}\left(l+\mathrm{ls}+z_k\right)f_0\sum_{j=k+1}^{n}\left(\sin\theta_k\sin\theta_j\cos^2\theta_j+\cos\theta_k\cos^3\theta_j\right) \\
+\frac{12}{m}\left(l+\mathrm{ls}+z_k\right)T\left(\sin\theta_n\cos\theta_k-\sin\theta_k\cos\theta_n\right)-\frac{12}{m}k_{\mathrm{t}}\left(\theta_k-\theta_{k-1}\right)+\frac{12}{m}k_{\mathrm{t}}\left(\theta_{k+1}-\theta_k\right) \\
-\sum_{j=1}^{n} A^{\theta_k}_{kj}\sin\left(\theta_k-\theta_j\right)\dot{\theta}_j^2 - 2\sum_{j=1}^{n-1} B^{\theta_k}_{kj}\cos\left(\theta_k-\theta_j\right)\dot{z}_j\dot{\theta}_j
\end{aligned}
\tag{37}
$$

- θ_n equation of motion for the TnT model

$$
\begin{aligned}
-6l\sin\theta_n\ddot{x}_1 + 6l\cos\theta_n\ddot{y}_1 + \sum_{j=1}^{n} A^{\theta_n}_{nj}\cos\left(\theta_n-\theta_j\right)\ddot{\theta}_j - \sum_{j=1}^{n-1} B^{\theta_n}_{nj}\sin\left(\theta_n-\theta_j\right)\ddot{z}_j \ &= \\
+\frac{12}{m}\frac{l}{2}f_0\left(\sin^2\theta_n\cos^2\theta_n+\cos^4\theta_n\right)-\frac{12}{m}k_{\mathrm{t}}\left(\theta_k-\theta_{k-1}\right) \\
-\sum_{j=1}^{n} A^{\theta_k}_{kj}\sin\left(\theta_k-\theta_j\right)\dot{\theta}_j^2 - 2\sum_{j=1}^{n-1} B^{\theta_k}_{kj}\cos\left(\theta_k-\theta_j\right)\dot{z}_j\dot{\theta}_j
\end{aligned}
\tag{38}
$$

with the new auxiliary coefficients

$$A_j^{xy} = \begin{cases} (n-1)\,(l+2l_s+2z_1) & \text{for } j=1 \\ [(2n-2j+1)l+2(n-j)l_s+2(n-j)z_1] & \text{for } j>1 \end{cases}$$

$$B_j^{xy} = 2(n-j)$$

$$A_{kj}^{z} = \begin{cases} (n-k)\,(l+2l_s+2z_1) & \text{for } j=1 \\ \left[2(n-k)l+2(n-k)l_s+2(n-k)z_j\right] & \text{for } 1<j\le k \\ \left[(2n-2j+1)l+2(n-j)l_s+2(n-j)z_j\right] & \text{for } j>k \end{cases}$$

$$B_{kj}^{z} = \begin{cases} 2(n-k) & \text{for } j\le k \\ 2(n-j) & \text{for } j>k \end{cases}$$

$$A_j^{\theta_1} = \begin{cases} 3(n-1)\,(l+2l_s+2z_1)^2+l^2 & \text{for } j=1 \\ 3\,(l+2l_s+2z_1)\left[(2n-2j+1)l+2(n-j)l_s+2(n-j)z_j\right] & \text{for } j>1 \end{cases}$$

$$B_j^{\theta_1} = 6\,(n-j)\,(l+2l_s+2z_1)$$

$$A_{kj}^{\theta_k} = \begin{cases} 3\,[(2n-2k+1)l+2(n-k)l_s+2(n-k)z_k]\,(l+2l_s+2z_1) & \text{for } j=1 \\ 6\left(l+l\mathrm{s}+z_j\right)[(2n-2k+1)l+2(n-k)l_s+2(n-k)z_k] & \text{for } 1<j<k \\ 6\,(l+l_s+z_k)\,(2(n-k)l+2(n-k)l_s+2(n-k)z_k]+4l^2 & \text{for } j=k \\ 6\,(l+l_s+z_k)\left[(2n-2j+1)l+2(n-j)l_s+2(n-j)z_j\right] & \text{for } j>k \end{cases}$$

$$B_{kj}^{\theta_k} = \begin{cases} 6\,[(2n-2k+1)l+2(n-k)l_s+2(n-k)z_k] & \text{for } j<k \\ 6\,[2(n-j)l+2(n-j)l_s+2(n-j)z_k] & \text{for } j\ge k \end{cases}$$

D. Numerical Methods

Before pressing on with the numerical implementation of each model, we first note that each set of ODEs can be rewritten in the more compact matrix form

$$\mathbf{M}(\mathbf{q}_m)\ddot{\mathbf{q}}_m = \mathbf{f}(t,\mathbf{q}_m,\dot{\mathbf{q}}_m) \tag{39}$$

where the subscript m attached to the generalised coordinate vectors in the above denotes the respective model being studied be it the rigid, torsion, or TnT lightsail model. As per numerical fashion, the second-order system described by equation (39) can readily be turned into a first-order system through the introduction of an auxiliary vector of unknowns $\boldsymbol{u} = \dot{\mathbf{q}}_m$. The above system can thus be rewritten in a more numerically friendly form

$$\hat{\mathbf{M}}(\mathbf{x})\dot{\mathbf{x}} = \hat{\mathbf{f}}(t,\mathbf{x}), \tag{40}$$

where

$$\hat{\mathbf{M}} = \begin{bmatrix} \mathbf{I} & \mathbf{0} \\ \mathbf{0} & \mathbf{M} \end{bmatrix}; \quad \hat{\mathbf{f}} = \begin{bmatrix} \mathbf{u} \\ \mathbf{f} \end{bmatrix}; \quad \mathbf{x} = \begin{bmatrix} \mathbf{q} \\ \mathbf{u} \end{bmatrix}.$$

Given the strong dependency of the modified mass matrix upon the numerical vector of unknowns x, the derivative of the unknown cannot be isolated in equation (40). This renders the use of more conventional ODE solvers inadequate, and thus to solve the numerical system of equation at hand we need to treat the set of first-order ODEs as a set of differential-algebraic equations (DAE) instead. Opting for solvers better adapted to tackle such DAEs, we first employ Mathematica's `NDSolve` solver package with the enforced "Residual" method of simplification whereby the `NDSolve` function first rewrites (40) into the fully implicit form

$$\hat{\mathbf{F}}(t,\mathbf{x},\dot{\mathbf{x}}) = \hat{\mathbf{M}}(\mathbf{x})\dot{\mathbf{x}} - \hat{\mathbf{f}}(t,\mathbf{x}) = \mathbf{0} \tag{41}$$

before proceeding with the numerical computation of the solution. The Mathematica results were then compared to the FORTRAN modified extended backward differentiation formulae (`MEBDFV`) solver written by Abdulla and Cash of Imperial College, London (Department of Mathematics). This `MEBDFV` solver was chosen because it deals precisely with systems of the form shown (40) with the mass matrix being strongly dependant upon the vector of unknowns and because numerical stability of its solution has been demonstrated on multiple occasions for the simulations of discrete mechanical systems similar to the present problem [19–21].

As its name implies, this `MEBDFV` solver employs a modified version of the backward differentiation formulae whereby, if $\mathbf{x}_i$ is the solution of the unknown at the current time step, a "superfuture" value, $\mathbf{x}_{i+1}$ is computed to improve computational stability by refining the initial guess of the derivative of the unknown, $\dot{\mathbf{x}}_i$, thereby allowing for a more accurate Newton-Raphson solution to the nonlinear system (41). For a concise description of the overall `MEBDFV` scheme, the reader is redirected to [21]. Naturally, the `MEBDFV` solver also includes additional intricacies such as adaptive time stepping and Newton-Raphson scheme convergence rate estimates, but their detailed description goes beyond the scope of this present paper. For a thorough treatise of the inner workings of the `MEBDFV` code, please refer to the papers written by Cash on the subject [22–25].

IV. Results and Discussion

A. Rigid Model Results

To quantitatively investigate the stability of the system, defects were introduced using sinusoidal initial perturbations of the form $a_0 \sin(2\pi\nu x/L)$ where a_0, the amplitude of perturbations, was set to 1.0 mm. Simulations were run for perturbation modes $\nu = \frac{1}{2}, 1, \frac{3}{2}, \ldots$ all the way through to five where the mode number is an indication of the number of complete sinusoidal cycles formed by the sail elements' initial positions (e.g., mode 3 implies the occurrence of 3 initial sinusoidal cycles). Fig. 5a shows an example of a mode $\frac{1}{2}$ initial perturbation. The simulations were run for a total of 10 ms and instability was considered to be achieved when the largest sail amplitude was greater than or equal to $2a_0$ – double the initial perturbation amplitude. The lightsail simulation properties were set for each run as follows:

1) Sail length, $L = 1$ m
2) Sail width, $W = 1$ m
3) Sail thickness, $h = 1$ µm
4) Sail density, $\rho = 1000\,\mathrm{kg/m^3}$, and
5) Impinging laser intensity, $I_0 = 100\,\mathrm{GW/m^2}$
6) Initial perturbation amplitude, $a_0 = 1.0$ mm
7) Number of elements, $n = 40$
8) Total runtime, $t_{\text{final}} = 10$ ms or to failure

All studied modes failed at troughs (see Fig. 5b) with the sole exception being perturbation mode 1/2 which only contains a crest. This mode appears to not precipitate the sail to failure (Fig. 5c-d). This is believed to be in part because of the mode's symmetry: All transverse components of the resultant laser loads appear to cancel out, leaving the system with only vertical force component tasked with the propulsion of the spacecraft. While this discovery of a stable mode is promising, perturbations do not occur in isolation in nature. A sail's microscopic defects are likely to consist of the superposition of multiple mode numbers. The instability of the troughs containing perturbations indicates that the sail, if left to its own devices, will crumple when subjected to the laser pressures required for rapid-transit propulsion. It thus remained necessary to study the influence of material strength upon the lightsail's structural stability.

B. Torsion Model Results

Given the rather large number of parameters required to perform a torsion model simulation, the theoretical expression for the critical lightsail material modulus $E_{\mathrm{cr_{max}}}$ was used as a guideline to reduce the parameter space to a more manageable size. As a result, only the material modulus, E, and the lightsail thickness, h were varied during the torsion model simulation runs. In particular, h was varied from 0.01 µm to 10 µm in jumps of powers of ten while the material modulus strayed only a few magnitudes away from its theoretical critical value. Each simulation was run for a total of 6 s using 30 elements and failure was once more considered whenever the perturbation amplitude doubled. Using 30 elements per simulation appeared justifiable first because the Euler-Bernoulli validation case showed appreciable convergence at the 30 element number mark (see Appendix subsection A) and second because, as a preliminary study, the need for the construction of a high resolution stability map was not yet needed. To further increase simulation speed,

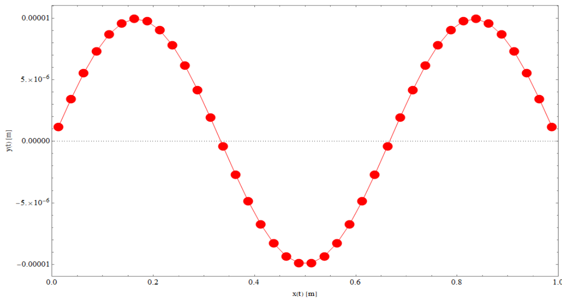

(a) Mode 3/2

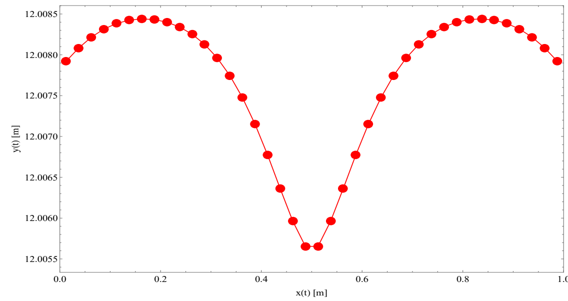

(b) Mode 3/2 at Failure

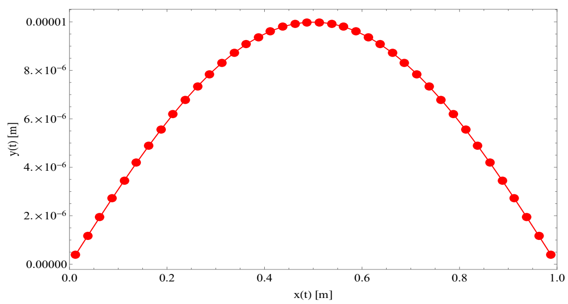

(c) Mode 1/2

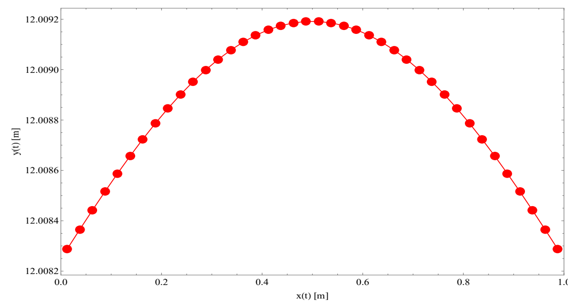

(d) Mode 1/2 after 10 ms

Fig. 5 Comparison between perturbation mode 3/2 (a) and mode 1/2 (c) simulations. Note the trough failure for mode 3/2 (b) and the absence of failure for mode 1/2 (d)

the radiation intensity and the initial amplitude of perturbation were tuned down from their previous rigid model values to $0.1\,\mathrm{GW/m^2}$ and 0.01 mm respectively. The new simulation properties are thus

1) Sail length, $L = 1$ m
2) Sail width, $W = 1$ m
3) Sail density, $\rho = 1000\,\mathrm{kg/m^3}$, and
4) Impinging laser intensity, $I_0 = 0.1\,\mathrm{GW/m^2}$
5) Initial perturbation amplitude, $a_0 = 0.01$ mm
6) Perturbation mode number, $\nu = 3/2$
7) Number of elements, $n = 30$
8) Total runtime, $t_{\mathrm{final}} = 6$ s or to failure

Figure 6 depicts the time evolution of the angular positions of a select number of elements for the $h = 1\,\mu\mathrm{m}/E = 4.5 \times 10^{13}$ Pa torsion model run where $E_{\mathrm{cr_{max}}} = 4.5 \times 10^{11}$ Pa. Give the quasi periodic nature of each element's angular position, the lightsail remained stable, that is, its initial perturbation amplitude never double during the runtime. Such lightsail configurations are termed "stable oscillatory". Figure 7, on the other hand, depicts the angular position of the elements for a torsion model run where $h = 1\,\mu\mathrm{m}/E = 4.5 \times 10^9$ Pa, i.e., a torsion model whose material modulus falls below its critical modulus. Notice that, after merely 2 seconds of runtime, the sail failed as indicated by the few elements whose angular position effectively blew up. One may object to calling such sample run unstable and claim it possible for the instability to have been caused by some form of numerical noise. That is a fair observation since, after all, if one zeros $h = 1\,\mu\mathrm{m}/E = 4.5 \times 10^{13}$ Pa angular position graph between $t = 0$ and $t = 100$ ms, the sail appears stable even though non-oscillatory (see Fig. 8). However, in the context of a stability study, it may just be that numerical noise acts as a simulation of physical noise. Given the uncertainty, runs such as these who do not exhibit stable oscillatory behavior, but eventually fail some time before runtime ends are termed "potentially unstable".

Figure 9 portrays a preliminary stability map of the torsion model wherein equation (8) is taken as reference (note that the axes are on a log-log scale). As previously mentioned, for each sail thickness from $0.01\,\mu\mathrm{m}$ to $10\,\mu\mathrm{m}$, the material modulus was varied only a few orders of magnitude away from the configuration's critical modulus. For example, for the $h = 1\,\mu\mathrm{m}$ case where $E_{\mathrm{cr_{max}}} = 4.5 \times 10^{11}$ Pa, the considered material modulus values were $E = \{4.5 \times 10^7$ Pa, 4.5×10^8 Pa, 4.5×10^9 Pa, 4.5×10^{13} Pa, 4.5×10^{14} Pa, 4.5×10^{15} Pa$\}$. Note whenever the

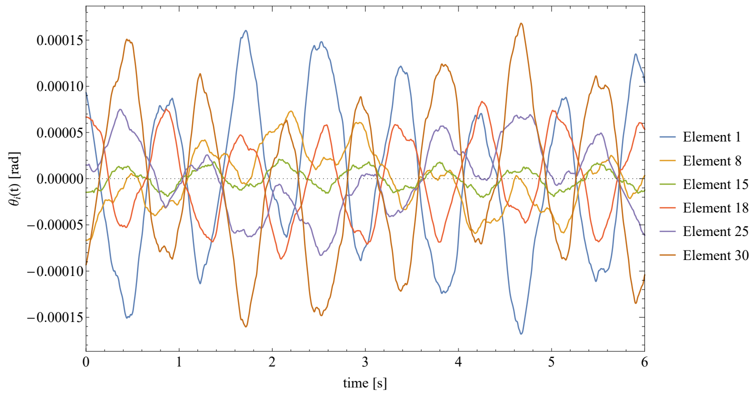

Fig. 6 Angular position of a select number of elements for the h = 1 µm/E = 4.5 × 10^{13} Pa case where $E_{\mathrm{cr}_{\max}}$ = 4.5 × 10^{11} Pa. Note the quasi-periodic behavior.

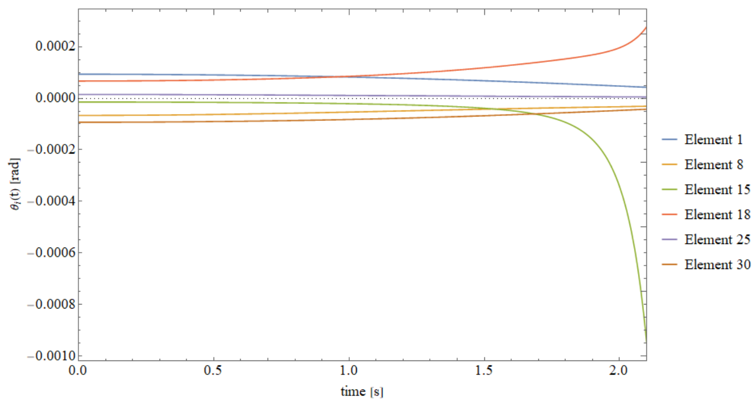

Fig. 7 Angular position of a select number of elements for the h = 1 µm/E = 4.5 × 10^{9} Pa case where $E_{\mathrm{cr}_{\max}}$ = 4.5 × 10^{11} Pa. Note how the angular coordinate of certain elements grows out of bound at failure.

material modulus value is a few orders of magnitude above its respective critical value, the lightsail exhibits stable oscillatory behavior. If the material modulus, on the other hand finds itself below its critical value, the lightsail becomes potentially unstable.

Because of the rather large values of material strength required for the lightsail to remain stable when its thickness is rendered small enough for practical interstellar travel, the torsion and tension lightsail FE model was next studied to investigate the effects of membrane action or tensile stiffness upon the lightsail's structural stability.

C. Torsion and Tension Model Results

As before with torsion model, the expression for $T_{\mathrm{cr}_{\max}}$ as derived from theory was used to make the parameter space of the TnT model more tractable. Consequently, only the boundary tension, T, the lightsail thickness, h, and the initial perturbations mode number, ν, were varied. In particular, ν took on the values 1, $\frac{3}{2}$, and 2 while, as in the torsion model case, h was varied from 0.01 µm to 10 µm in jumps of powers of ten while the boundary tension was varied by only a few magnitudes away from its theoretical critical value. Note also that, in order to solely investigate the influence of membrane action or tensile stiffness upon the lightsail structural stability, the bending stiffness of the lightsail model was manually tuned down to 0 by setting $k_T = 0$ (although, because of the dependency of bending stiffness upon h^3, the presence or absence of torsional springs hardly made a difference given the range of the thickness values studied). Once more, each simulation was run for a total of 6 seconds using 30 elements and failure was considered to have occurred when the light-sail perturbation amplitude doubled. The simulation properties were as listed below:

1) Sail length, L = 1 m
2) Sail width, W = 1 m

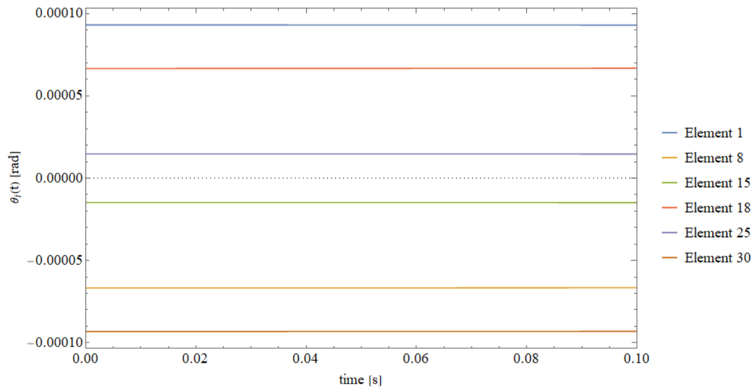

Fig. 8 Zero in of the angular position vs time graph of the (h = 1 μm, E = 4.5 × 10^9 Pa). Had the simulation been run for only 100 ms, this case may have been deemed stable.

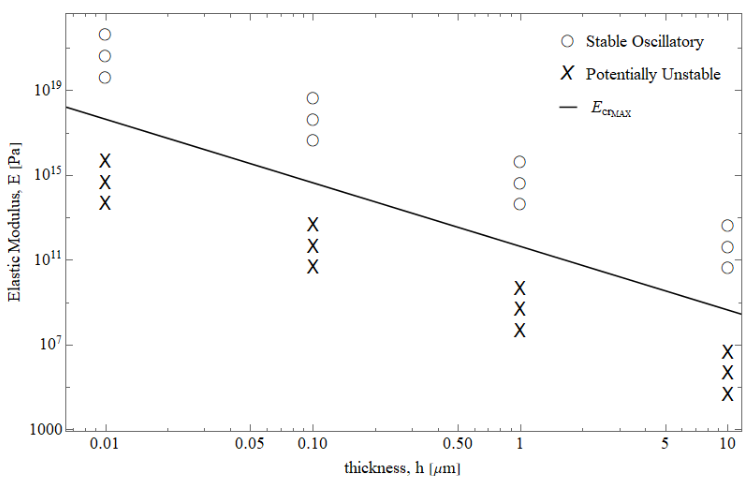

Fig. 9 Low resolution stability map for the torsion model study cases. Note the log-log scale

3) Sail density, $\rho = 1000\,\mathrm{kg/m^3}$, and
4) Impinging laser intensity, $I_0 = 0.1\,\mathrm{GW/m^2}$
5) Initial perturbation amplitude, $a_0 = 0.01$ mm
6) Number of elements, $n = 30$
7) Total runtime, $t_{\text{final}} = 6$ s or to failure.

Figure 10 shows the angular position of a few of the elements of the lightsail TnT run with values $h = 1\,\mu\mathrm{m}/T = 3.34 \times 10^{-3}\,\mathrm{N}/\nu = \frac{3}{2}$ where $T_{\mathrm{cr}_{\max}} = 3.34 \times 10^{-6}$ N. As in the bending stiffness case, the simulation of a lightsail whose boundary tension magnitude is above that of its critical tension value exhibits stable oscillatory motion. Conversely, decreasing boundary tension value a few orders of magnitude below the critical value like, say, letting $T = 3.34 \times 10^{-8}$ N in the previous $h = 1\,\mu\mathrm{m}/\nu = \frac{3}{2}$ scenario makes it so that the lightsail becomes potentially unstable (see Fig. 11). Figure 12 shows a low resolution of the stability parameter map for the $\nu = \{1, \frac{3}{2}, 2\}$ cases for various values of h. Given that the mode number, ν, largely unaffected the critical tension threshold, only one plot/map was required for all three mode numbers under study.

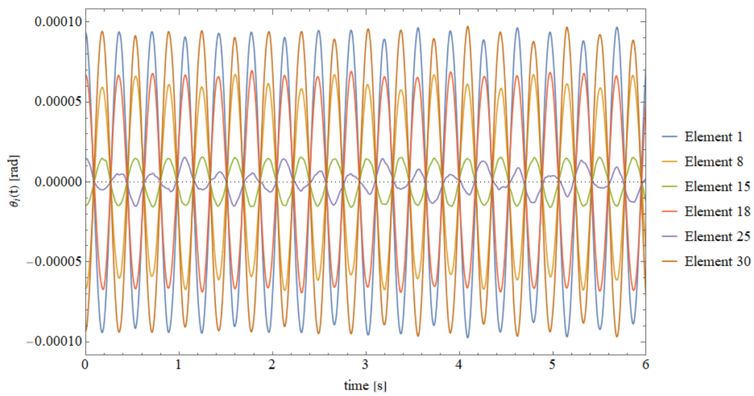

Fig. 10 Angular position of a select number of elements for the $h = 1\,\mu\mathrm{m}/T = 3.34 \times 10^{-3}\,\mathrm{N}/\nu = \frac{3}{2}$ case where $T_{\mathrm{cr}_{\max}} = 3.34 \times 10^{-6}$ N. Note once more the quasi-periodic behavior.

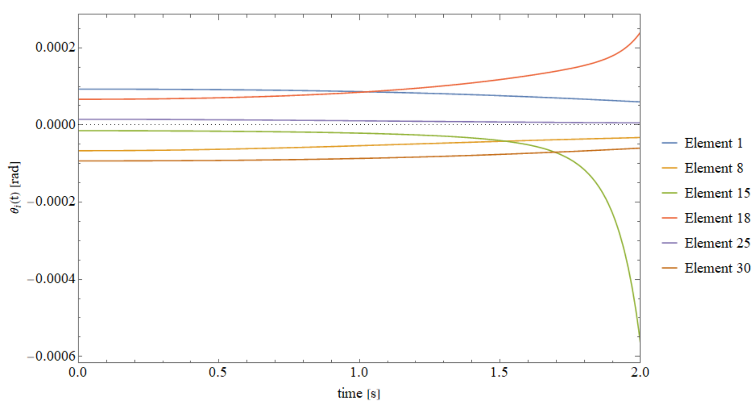

Fig. 11 Angular position of a select number of elements for the $h = 1\,\mu\mathrm{m}/T = 3.34 \times 10^{-8}\,\mathrm{N}/\nu = \frac{3}{2}$ case where $T_{\mathrm{cr}_{\mathrm{m}}\mathrm{athrmmax}} = 3.34 \times 10^{-6}$ N. Failure occurred at roughly 2 seconds.

Given the practical magnitudes ($T_{\mathrm{cr}_{\max}} \sim 10^{-6}$ N) of the require applied tension value for certain stability to occur, the authors deem it pertinent for the reader to get a more detailed view at the trends of the TnT model within both the stable oscillatory and potentially unstable regimes. See Appendix section C for the figures that follow. Figure 18 showcases how increasing the magnitude of the boundary when the lightsail finds itself in the stable oscillatory regime increases its vibrational frequency of oscillations. Conversely, decreasing the lightsail thickness when the boundary tension magnitude is above that of the critical value also increases the lightsail's frequency of vibrations (Fig.19).

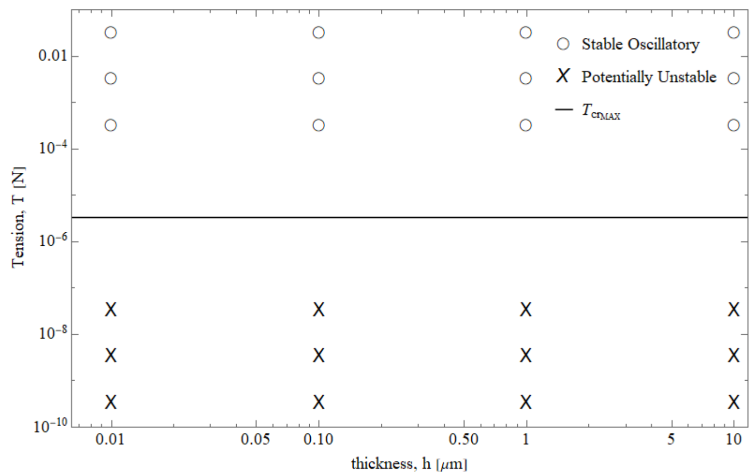

Fig. 12 Low resolution stability map for the tension model study cases. Note the log-log scale

Although it is unclear whether changing the mode number increases or decreases the frequency of oscillations when in the stable regime, Fig.20 makes it clear that the shape of the lightsail's angular oscillations change as the mode number is changed (as one would expect). Further when in the potentially unstable regime, lowering the boundary tension value and changing the mode number appear to have no significant influence on the time when the lightsail fails (see Figures 21 and 22). However, Fig. 23 clearly shows that decreasing the lightsail thickness when in the potentially unstable regime drastically speeds up the occurrence of failure.

D. Numerical Model Limitations

It remains of note that the numerical models and results studied thus far hold certain limitations. For once the actual intensity profile of a laser beam varies according to a Gaussian distribution. Here, the laser beam intensity was taken as uniform and the actual non-uniformity of a Gaussian beam may cause additional stability strains. Further, and perhaps of greater importance, is the fact to no lightsail FE model included the presence of heat dissipation. This is especially important given the stable oscillatory behavior of the torsion and TnT models when above their respective $E_{cr_{max}}$ and $T_{cr_{max}}$ values. In particular, it was noted that further increasing the boundary tension beyond its critical value increased the frequency of oscillations of the lightsail's perturbations. Increasing frequency of oscillation in the presence of dissipation effects can potentially increase the internal heat generation to a point where the lightsail may melt even absent any radiation absorption. Finally, each sail element was modeled as perfectly reflective, only, as noted by [7, 8], the material diffraction property can potentially be used to help enforce lightsail stability. In order to improve the physical accuracy of the lightsail model it will be thus necessary in the future to include:

1) a Gaussian laser beam intensity distribution,
2) heat dissipation effects, and
3) material optics properties.

V. Conclusion

The large directed energy loads required for laser-driven propulsion pose the problem of the stability of the lightsail shape. Given the unavoidable presence of microscopic defects along the reflective foil's surface, it is an imperative to determine whether the sail will retain its shape or crumple under large photon pressures. An analytical theory of stability was first proposed wherein critical values for the material modulus, E_{cr}, and for boundary tension, T_{cr}, are derived from certain key lightsail parameters such as thickness and laser intensity. The analytical model was juxtaposed against various numerical models. In the absence of boundary tension, both theory and numerical simulations predict the necessity of very large elastic moduli to guarantee the lightsail's stability. Increasing the sail thickness can potentially generate stable sail configurations, but to the detriment of spacecraft acceleration. With the addition of boundary tension, it was found from both theory and numerical simulations that the lightsail can be kept under a stable oscillatory state through the application of relatively small tensile loads even for small lightsail thicknesses. The preliminary parameter maps provided by the analytical theory and verified through numerical simulation could potentially provide the mission designer with a convenient method to engineer a lightsail capable of sustaining the large directed laser pressures needed for high-acceleration spacecraft applications.

Appendix

This Appendix documents the methods used to validate the various lightsail FE models. In particular, this appendix contains the Euler-Bernoulli beam validation case for the torsional lightsail model and the G3 guitar string validation case for the TnT model. Also, section C of the Appendix contains some relevant graphs referred to in the results section.

A. Euler-Bernoulli Beam Validation

Given that the torsion lightsail model was constructed specifically to account for material bending stiffness in the elastic regime, a fitting validation case here is that of the classic Euler-Bernoulli cantilever beam. The beam, held fixed at its left end sustains an applied concentrated load P at its right end (see Fig. 42). The Euler-Bernoulli theory predicts, for small deformations, the deflection

$$\delta(x) = \frac{P_0 x^2}{6EI}(x - 3L). \tag{42}$$

The setup for the numerical simulation is much akin to the torsion lightsail model with only a few minor exceptions to account for applied forces and boundary conditions. Since the left end is fixed, the coordinate of the center of mass of the first element is set to $(x_1 = \frac{l}{2}, y_1 = 0)$ and the angular position of the first element is held fixed at $\theta_1(t) = 0$. This, in turn, reduces the size of the system of equations from $n + 2$ to $n - 1$. Finally, the radiation loads $\mathbf{f}_i$ are set to 0 and replaced by a static concentrated force, $P(t)$ applied at the last element's center of mass (x_n, y_n). This new FE model can be seen in Fig. 15b.

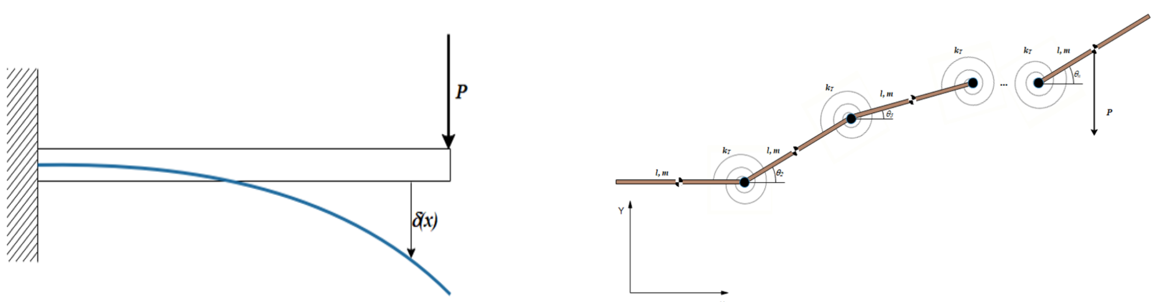

(a) (b)

Fig. 13 Euler-Bernoulli validation setup; (a) depicts the continuous beam and (b) the discrete model.

To properly simulate static loading, the applied transverse load is of the form

$$P(t) = P_0\left(1 - e^{-t/\tau}\right), \tag{43}$$

that is, the applied load is slowly increased from zero at time $t = 0$ to its final value P_0 at the end of the simulation. In the above, τ stands for the time-constant of the applied static load. For the purposes of validation, we here set $P_0 = 100\,\text{N}$ and $\tau = 0.3\,\text{s}$ and run each simulation for a total of 2 seconds. The applied force $P(t)$ is graphed in Fig. 14.

The simulation parameters for the beam validation where are listed below

1) Beam length, $L = 1\,\text{m}$;
2) Beam thickness, $h = 0.2\,\text{m}$;
3) Beam width, $W = 0.1\,\text{m}$;
4) Beam density (steel), $\rho = 7800\,\text{kg/m}^3$; and
5) Beam modulus (steel), $E = 200\,\text{GPa}$.

Note that, given the specifications written above, the beam validation moment of area is here $I = \frac{1}{12}Wh^3$. The simulations were run for different number of elements and the maximum error between the analytical $\delta(x)$ deflection

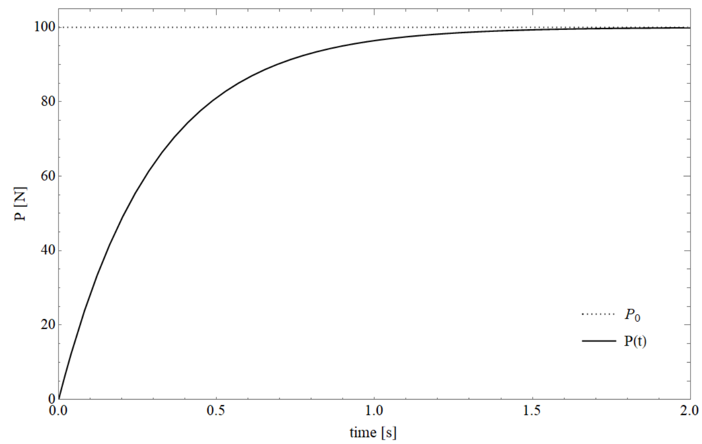

Fig. 14 Applied transverse load $P(t)$ as a function of time.

and the numerical beam deflection at end of runtime was computed for each run by taking the difference between the absolute difference between a given element's vertical end coordinate and its theoretical deflection:

$$e_{EB_{\max}} = max\left(\left|\delta(x_j(t_{end}) - y_j(t_{end})\right|\right) \text{ for } i = 1,\ 2,\ 3,\ \ldots,\ n \tag{44}$$

Figure 15 contains a plot of the maximum absolute error vs the number of elements alongside a depiction of the analytical and numerical beam deflections for $n = 30$. Note that, after $n = 30$, the absolute maximum error seems to have plateaued to $e_{EB_{\max}} = 1.84 \times 10^{-7}$ m. This plateau discrepancy is suspected to be due to how the static force $P(t)$ tends, as time progresses, towards P_0, but never quite fully reaches it, hence why the numerical model would settle down to a slightly smaller deflection curve. Nevertheless, the very small error between theory and numerics certainly helps build confidence into the validity of the lightsail torsion model.

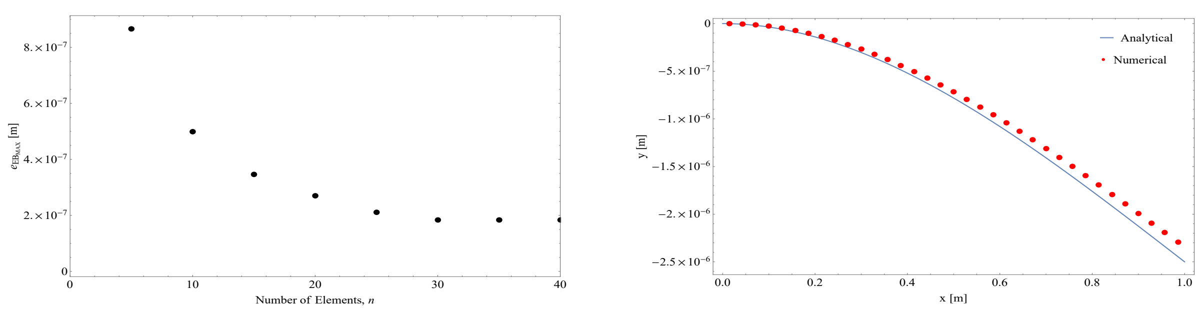

(a) **(b)**

Fig. 15 Euler-Bernoulli cantilever beam validation results; (a) showcases the error convergence plot and (b) compares the analytical and numerical results for 35 elements.

B. G3 Guitar String Validation

Given its inclusion of rectilinear springs and boundary tension, a pertinent scenario to validate the TnT model against is that of a musical string's harmonics. From Newtonian first principles, it is known that the fundamental frequency, f_0, of a string under constant tension, T, and kept fixed at both ends can be expressed as

$$f_0 = \frac{1}{2L}\sqrt{\frac{TL}{M}} \tag{45}$$

where L is the working length, that is, stretched length of the string and M is its total mass. Here, a guitar G3 string with a fundamental frequency of $f_{0_{G3}} = 196.00$ Hz was chosen for the purpose of validating the TnT model. Given the guitar string manufacturer D'Addario's specification for conventional acoustic guitar G3 strings, the simulation parameters for the guitar string validation are as follows:

1) String length, $L = 0.6477\,\mathrm{m}$;
2) String gauge (diameter), $d = 0.430\,\mathrm{mm}$;
3) String density (piano wire), $\rho = 7800\,\mathrm{kg/m^3}$; and
4) String modulus (piano wire), $E = 210\,\mathrm{GPa}$.

In this particular, string case, the cross-sectional area of the numerical model and its second moment of area are, respectively, $A_c = \frac{\pi d^2}{4}$ and $I = \frac{\pi}{4}\left(\frac{d}{2}\right)^2$. With the above specifications, then tension that needs be applied to the string to obtain the G3 frequency can readily be computed using equation (45) to be $T = 72.485\,\mathrm{N}$. In adapting the TnT model to the taunt string scenario, one comes across a peculiar problem. In order to keep right end of the TnT model fixed, it is not enough to simply set y_n = constant. This holonomic constraint would, in turn, eliminate the connection between the last TnT element and the remainder of the string. It would be as though the hinge connecting the last extensible element to the other elements was deleted at the start of the simulation. Ideally, one would want the vertical acceleration component of the last element to be zero throughout the simulation, that is, ideally, $\ddot{y}_n(t) = 0$. In reality, however, $\ddot{y}_n = f(\mathbf{q}, \dot{\mathbf{q}})$, and, in fact, $\ddot{y}_n$ is strongly non-linear in $\mathbf{q}$, thus we cannot use Lagrangian multipliers to account for the generalized force(s) needed to maintain the $\ddot{y}_n(t) = 0$ constraint. Fortunately, maintaining the first string element fixed, that is, setting (x_1 = constant, y_1 = constant) and ensuring that the two applied boundary tension forces remain co-linear with their respect element, that is, enforcing $\mathbf{T}_1 = T(-\cos\theta_1, -\sin\theta_1, 0)$ and $\mathbf{T}_n = T(\cos\theta_n, \sin\theta_n, 0)$ appears to keep the end element from straying too much from its starting position.

Because we seek to verify that the fundamental frequency of the simulated string is indeed that of a G3 string, we chose to initially deformed the string in a half sine wave fashion where $y(x) = a_0 \sin\left(\frac{\pi x}{L}\right)$ where, here, $a_0 = 0.1\,\mathrm{mm}$. Further, to simulate pre-tension, the initial elongation of each rectilinear spring is set such that they each exert a total force equal in magnitude to the boundary tension, that is, we set $z_i = T/k_s$ for $i = 1, 2, 3 \ldots, n-1$.

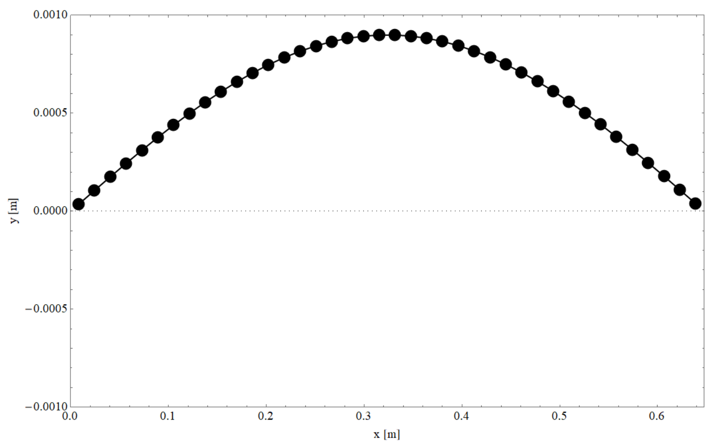

Fig. 16 Lightsail guitar string validation model initial deformations for n = 40.

Figure 17 below showcases the validation results. To properly measure the initially deformed string's fundamental frequency, the frequency of vertical oscillations of each string element with the exception of the ends was measured via a discrete Fourier transform (DFT). The mean fundamental frequency of the total elements is plotted in Fig. 17a. Note that, as per theory, each element ended up oscillating with the same frequency and thus the standard deviation from the mean is always zero, hence the absence of error bars in Fig. 17a. The mean fundamental frequency of the string appears to have settled, after the number of elements has been increased to 6, to that of 199.96 Hz which is less than 3 Hz from the fundamental frequency of a G3 string. The discrepancy is suspected to be due at least in part to the DFT scheme and perhaps in part also due to the "wobbling" of the nth element. Figure 17b portrays the maximum amplitude of the vertical oscillations of the nth element. Note that the wobbling of the nth element steadily tends to disappear as the number of elements is increased.

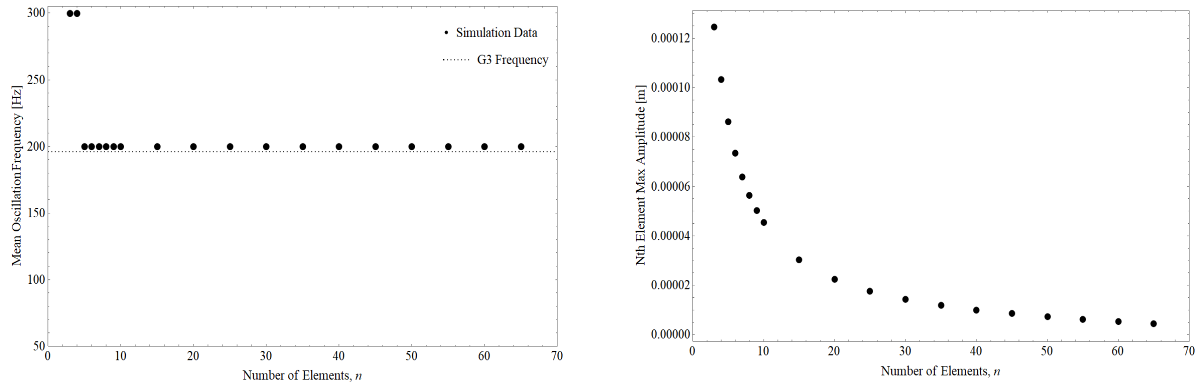

(a) **(b)**

Fig. 17 Guitar string validation results.

C. Relevant Figures

The following figures describe the trends followed through by the Tension model as key parameters varied in value. The first three figures pertain to the stable oscillatory regime tendencies whereas the last three pertain to the unstable regime.

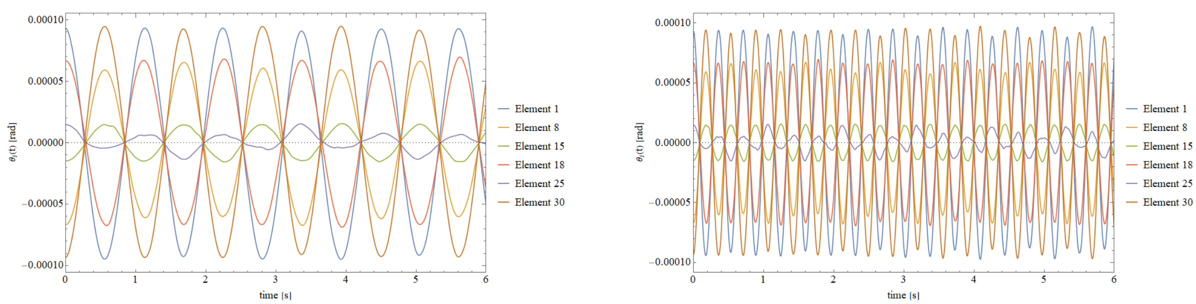

(a) $T = 3.34 \times 10^{-4}$ N **(b)** $T = 3.34 \times 10^{-3}$ N

Fig. 18 Varying tension magnitude for the ($h = 1\ \mu$m; $\nu = \frac{3}{2}$) stable study case.

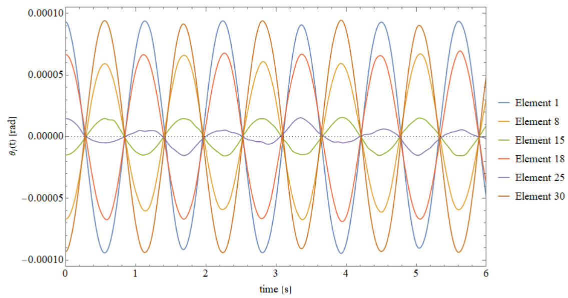

(a) $h = 10\,\mu\mathrm{m}$

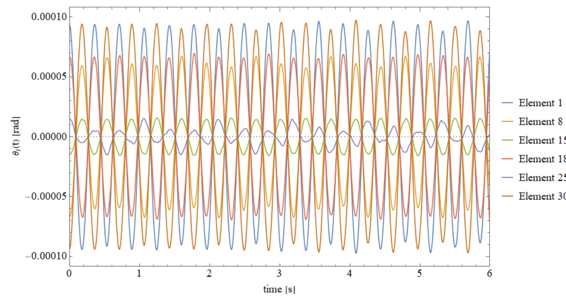

(b) $h = 1\,\mu\mathrm{m}$

Fig. 19 Varying thickness, h, for the ($T = 3.34 \times 10^{-3}$ N; $\nu = \frac{3}{2}$) study case.

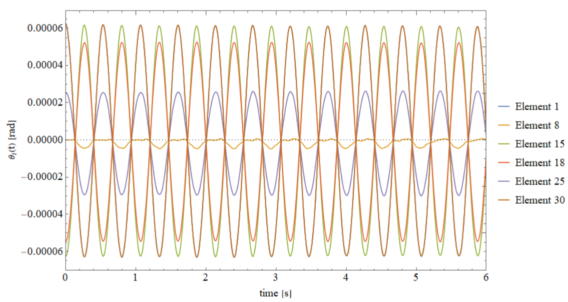

(a) $\nu = 1$

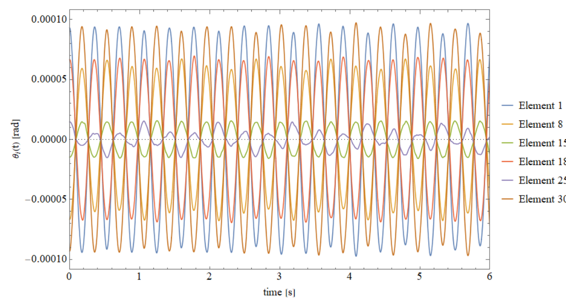

(b) $\nu = \frac{3}{2}$

Fig. 20 Varying the mode number, ν, for the ($T = 3.34 \times 10^{-3}$ N; $h = 1\,\mu$m) study case.

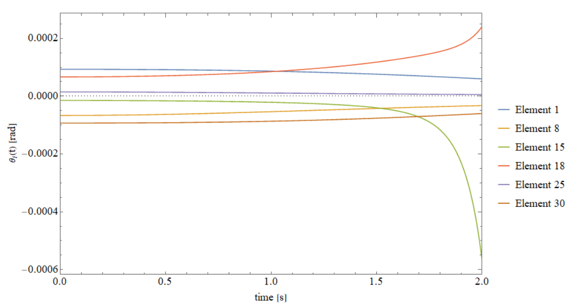

(a) $T = 3.34 \times 10^{-8}$ N

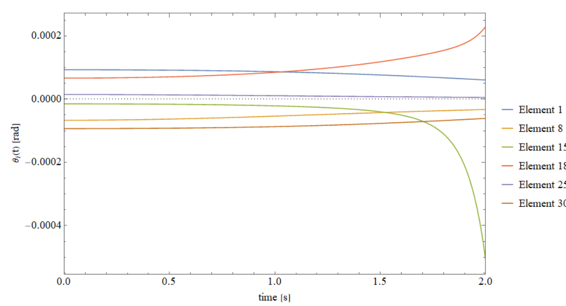

(b) $T = 3.34 \times 10^{-9}$ N

Fig. 21 Varying tension magnitude for the ($h = 1\,\mu$m; $\nu = \frac{3}{2}$) unstable study case.

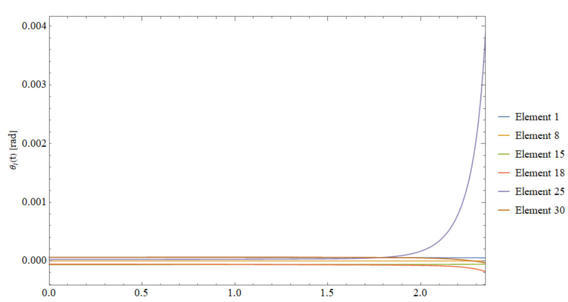

(a) $\nu = 1$

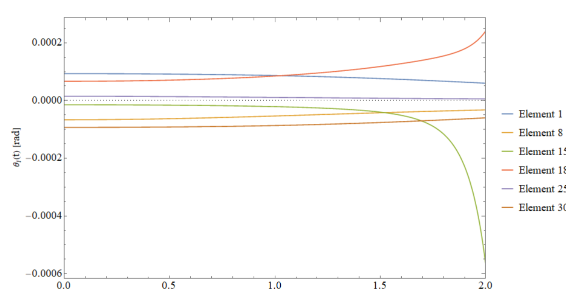

(b) $\nu = \frac{3}{2}$

Fig. 22 Varying the mode number, ν, for the ($T = 3.34 \times 10^{-8}$ N; $h = 1\,\mu$m) study case.

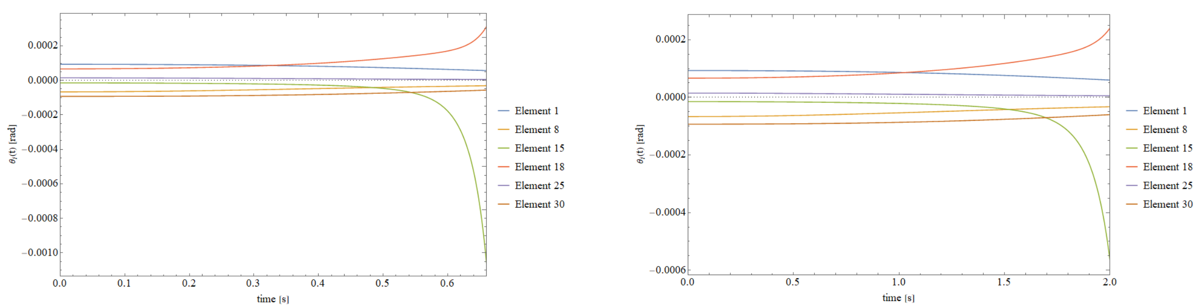

(a) $h = 0.1\,\mu\text{m}$

(b) $h = 1\,\mu\text{m}$

Fig. 23 Varying thickness, h, for the ($T = 3.34 \times 10^{-8}\,\text{N}$; $\nu = \frac{3}{2}$) study case. Note how failure happens much faster when the value of h is decreased.

Acknowledgments

The work described in this paper is supported by Natural Sciences and Engineering Research Council of Canada (NSERC) and the McGill Summer Undergraduate Research in Engineering Program.

References

[1] Forward, R. L., "Roundtrip interstellar travel using laser-pushed lightsails," *Journal of Spacecraft and Rockets*, Vol. 21, No. 2, 1984, pp. 187–195.

[2] Lubin, P., "A Roadmap to Interstellar Flight," *Journal of the British Interplanetary Society*, Vol. 69, 2016.

[3] Parkin, K. L., "The breakthrough starshot system model," *Acta Astronautica*, Vol. 152, 2018, pp. 370–384.

[4] Manchester, Z., and Loeb, A., "Stability of a light sail riding on a laser beam," *The Astrophysical Journal Letters*, Vol. 837, No. 2, 2017, p. L20.

[5] Srinivasan, P., Hughes, G. B., Lubin, P., Zhang, Q., Madajian, J., Brashears, T., Kulkarni, N., Cohen, A., and Griswold, J., "Stability of laser-propelled wafer satellites," *Planetary Defense and Space Environment Applications*, Vol. 9981, International Society for Optics and Photonics, 2016, p. 998105.

[6] Atwater, H. A., Davoyan, A. R., Ilic, O., Jariwala, D., Sherrott, M. C., Went, C. M., Whitney, W. S., and Wong, J., "Materials challenges for the Starshot lightsail," *Nature Materials*, Vol. 17, No. 10, 2018, pp. 861–867.

[7] Srivastava, P., and Swartzlander, G., "Optomechanics of a stable diffractive axicon light sail," *The European Physical Journal Plus*, Vol. 135, 2020. https://doi.org/10.1140/epjp/s13360-020-00542-1.

[8] Ilic, O., and Atwater, H., "Self-stabilizing photonic levitation and propulsion of nanostructured macroscopic objects," *Nature Photonics*, Vol. 13, 2019. https://doi.org/10.1038/s41566-019-0373-y.

[9] Sakamoto, H., Miyazaki, Y., and Park, K. C., "Finite Element Modeling of Sail Deformation Under Solar Radiation Pressure," *Journal of Spacecraft and Rockets - J SPACECRAFT ROCKET*, Vol. 44, 2007, pp. 514–521. https://doi.org/10.2514/1.23474.

[10] Huang, X., Zeng, X., Circi, C., Vulpetti, G., and Qiao, D., "Analysis of the solar sail deformation based on the point cloud method," *Advances in Space Research*, 2020. https://doi.org/10.1016/j.asr.2020.05.008.

[11] Liu, J., Rong, S., Shen, F., and Cui, N., "Dynamics and Control of a Flexible Solar Sail," *Mathematical Problems in Engineering*, Vol. 2014, 2014. https://doi.org/10.1155/2014/868419.

[12] Wong, W., and Pellegrino, S., "Wrinkled membranes Part I: Experiments," *Journal of Mechanics of Materials and Structures - J MECH MATER STRUCT*, Vol. 1, 2006, pp. 3–25. https://doi.org/10.2140/jomms.2006.1.3.

[13] Wong, W., and Pellegrino, S., "Wrinkled Membranes, Part II: Analytical Models," *Journal of Mechanics of Materials and Structures - J MECH MATER STRUCT*, Vol. 1, 2006, pp. 27–61. https://doi.org/10.2140/jomms.2006.1.27.

[14] Wong, W., and Pellegrino, S., "Wrinkled membranes. Part III: Numerical simulations," *Journal of Mechanics of Materials and Structures - J MECH MATER STRUCT*, Vol. 1, 2006, pp. 63–95. https://doi.org/10.2140/jomms.2006.1.63.

[15] YW, W., Pellegrino, S., and Park, K. C., "Prediction of Winkle Amplitudes in Square Solar Sails," 2003. https://doi.org/10.2514/6.2003-1982.

[16] Cassenti, B., Matloff, G., and Strobl, J., "The structural response and stability of interstellar solar sails," *Journal of the British Interplanetary Society*, Vol. 49, No. 9, 1996, pp. 345–350.

[17] Genta, G., and Riccobono, D., "Preliminary Analysis of the Deformed Shape of an Inflated Light Sail," *5th Tennessee Valley Interstellar Workshop (TVIW), Huntsville (Alabama, USA)*, 2017.

[18] Myrabo, L. N., Knowles, T. R., Bagford, J. O., and Seibert II, D. B., "Experimental investigation of laser-pushed light sails in a vacuum," *High-Power Laser Ablation III*, Vol. 4065, International Society for Optics and Photonics, 2000, pp. 521–532.

[19] Fritzkowski, P., and Kaminski, H., "A discrete model of a rope with bending stiffness or viscous damping," *Acta Mechanica Sinica/Lixue Xuebao*, Vol. 27, 2011, pp. 108–113. https://doi.org/10.1007/s10409-011-0417-0.

[20] Fritzkowski, P., and Kaminski, H., "Dynamics of a Rope as a Rigid Multibody System," *Journal of Mechanics of Materials and Structures*, Vol. 3, 2008, pp. 1059–1075. https://doi.org/10.2140/jomms.2008.3.1059.

[21] Fritzkowski, P., and Kamiński, H., "Dynamics of a rope modeled as a discrete system with extensible members," *Computational Mechanics*, Vol. 44, 2009, pp. 473–480. https://doi.org/10.1007/s00466-009-0387-2.

[22] Cash, J., and Considine, S., "An MEBDF code for stiff initial value problems," *ACM Transactions on Mathematical Software (TOMS)*, Vol. 18, 1992, pp. 142–155. https://doi.org/10.1145/146847.146922.

[23] Cash, J., "Modified extended backward differentiation formulae for the numerical solution of stiff initial value problems in ODEs and DAEs," *Journal of Computational and Applied Mathematics - J COMPUT APPL MATH*, Vol. 125, 2000, pp. 117–130. https://doi.org/10.1016/S0377-0427(00)00463-5.

[24] Abdulla, T., Cash, J., and M.T.Diamantakis, "An MEBDF package for the numerical solution of large sparse systems of stiff initial value problems," *Computers Mathematics with Applications*, Vol. 42, 2001, pp. 121–129. https://doi.org/10.1016/S0898-1221(01)00137-7.

[25] Cash, J., "Review Paper: Efficient numerical methods for the solution of stiff initial-value problems and differential algebraic equations," *Royal Society of London Proceedings Series A*, Vol. 459, 2003, pp. 797–815. https://doi.org/10.1098/rspa.2003.1130.